

TRAVERSABILITY OF HOPPING ROVERS ON SMALL SOLAR SYSTEM BODIES

Benjamin Hockman and Marco Pavone

Dept. of Aeronautics and Astronautics, Stanford University, Stanford, CA. 94305, b.hockman@stanford.edu

ABSTRACT

In this paper we explore notions of *traversability* for hopping rovers on small solar system bodies, such as asteroids and comets, with a focus on developing actionable tools for mission planning. We start with a discussion of hopping dynamics and the inherent differences between notions of “traversability” for hopping and traditional wheeled rovers. We then discuss various map-based tools for understanding the surface gravity environment and propose an algorithm that partitions the surface into locally traversable regions. Finally, we leverage dynamic simulations to estimate k -hop backwards reachable sets—that is the surface regions from which a particular point can be reached within k hops. A case study of comet 67P demonstrates that even extremely irregular bodies may be largely traversable with an appropriate hopper design.

1 INTRODUCTION

Small solar system bodies such as comets and asteroids have become high priority targets for planetary exploration. Driven by scientific interest, planetary defense, and the potential for resource extraction, missions to small bodies are continuing to advance our understanding of their origin, evolution, and chemistry. However, a more detailed characterization of their composition and physical properties requires direct contact with the surface at multiple locations for an extended period of time [1]. Accordingly, various surface landers and rovers have been studied for small bodies, which must contend with, among other challenges, an extremely weak gravity field. In November 2014, the Rosetta spacecraft deployed a 100 kg lander named Philae to the surface of comet 67P, which touched down at 1 m/s and bounced over 1 km off target, illustrating the challenge of remaining grounded in microgravity [2]. Thus, *hopping* has become a popular mobility concept for microgravity rovers, which exploits this tendency to lose surface contact. Indeed, four small hopping rovers are currently en route to Asteroid Ryugu aboard the Hayabusa 2 spacecraft: a 10 kg MASCOT rover developed by DLR and three 500 g MINERVA landers developed by JAXA, each equipped with an internal “momentum device” for self-righting and to perform small hops, albeit with minimal control [3].

Other rover architectures are being developed to enhance the controllability and autonomy of hopping and enable science investigations that require targeted, point-to-point mobility. “Hedgehog,” a rover under development by the authors, is one such platform that has demonstrated an unprecedented level of mobility precision through experiments in various gravity-offloading test beds [4, 5]. With

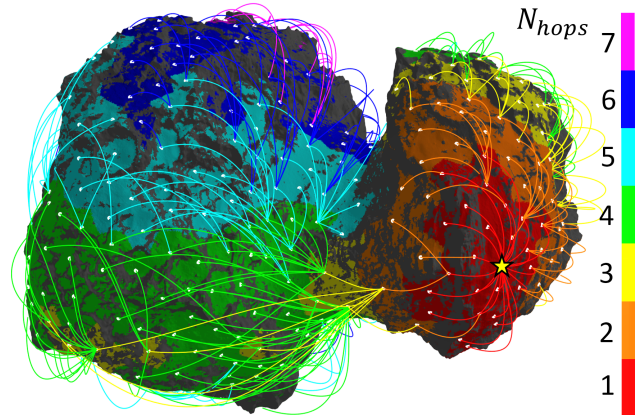


Figure 1: This paper proposes several tools for analyzing the traversability of hopping rovers. Shown here is a plot of backwards reachable sets from a point on comet 67P.

the ability to control the direction and speed of hops and through an iterative autonomy architecture that allows the rover to correct for erratic bouncing in subsequent maneuvers, Hedgehog has the potential to achieve meter-scale mobility precision, even over long, km-scale traverses.

However, in addition to their microgravity, another defining characteristic of many small bodies is their irregular shape and rough terrain, which poses an additional challenge for assessing the *traversability* of a hopping rover. In fact, the notion of “traversable terrain” assumes a very different meaning for hoppers than for traditional wheeled rovers, as hoppers can, for example, bypass difficult terrain and reach locations that would otherwise be inaccessible to surface-bound rovers (e.g. hopping directly out of a crater rather than climbing its walls). Thus, traditional methods for traversability analysis and mission planning for wheeled rovers are not directly applicable to hopping rovers.

Statement of contributions: The goal of this paper is to investigate traversability for hopping rovers, with a particular focus on developing actionable tools for mission planning. We first review the dynamics of hopping rovers as they relate to characterizing feasible hopping trajectories and uncertainty. We then discuss various map-based tools for understanding the surface gravity environment and propose an algorithm that partitions the surface into locally traversable regions. Finally, we leverage dynamic simulations to estimate k -hop backwards reachable sets—that is the surface regions from which a particular point can be reached within k hops. A case study of comet 67P demonstrates that even extremely irregular bodies may be largely traversable with an appropriate hopper design.

2 BACKGROUND

For Mars rovers, landing site selection is aided by a traversability analysis derived from high resolution orbital imagery, which is processed to classify terrain types, estimate rock abundance, and compute digital elevation models (DEM) of the surface [6]. Once deployed, rovers then use their onboard cameras to estimate local traversability more accurately for their next mobility sequence [7]. In general, rocks, loose regolith, and steep slopes ($> 20^\circ$) are deemed obstacles, and the rover then plans a path to its next waypoint within the free space.

However, hopping rovers have two fundamental differences with respect to traditional wheeled rovers: (1) their off-surface degree of freedom, and (2) and their discontinuous interaction with the environment through intermittent, impulsive hops. While seemingly obvious, these differences have profound implications for assessing traversability. Chiefly, the *path* of a hopping rover is defined by a series of points on the surface that the rover hops between rather than a continuous trajectory, which allows it to access locations that are surrounded by unfavorable terrain (e.g. a plateau or crater with a steep perimeter). In other words, a feasible path need not be composed of a continuous series of feasible sub-paths—a fundamental axiom of traditional surface mobility. However, the nature of sparse control inputs also prohibits a hopper from tracking a planned trajectory during ballistic flight, whereby errors in hop execution and the dynamics model may cause it to drift off course from its intended landing site.

In the case where a rover may experience highly elastic and uncontrolled impacts with the surface, the landing uncertainty can be quite large. Previous work by the authors has explored how reinforcement learning (RL) techniques may be used to *learn* hopping control policies from simulated trajectory data that includes stochastic bouncing dynamics [8]. While this approach can account for a large degree of stochasticity in the dynamics, control policies derived solely from data are not immediately generalizable to other objectives (e.g. target locations) and can be expensive to compute. Therefore, this RL approach is not particularly useful in the context of mission planning, where rapid point-to-point traversability queries are required.

However, in many cases, bounces may be small, for example if the surface regolith has considerable damping or the hopper itself has some means of dissipating impact energy. In these cases, the hopper is much more likely to land within a close vicinity to the nominal landing site and the overall motion is primarily governed by the initial hopping trajectory rather than subsequent bounces. This assumption allows more direct methods to be used for studying traversability, such as considering the two-point boundary value problem. In Sect. 5, we utilize the Lambert solver developed by [8] to form a graph of trajectories between a set of sampled points, which is then used to extract trajectory trees to or from any point on the surface.

While there have been many previous studies investigating

the design of hopping architectures, very little work exists concerning motion planning and global traversability. For the deployment of small landers such as MINERVA, Monte Carlo simulations have been used to characterize landing distributions [8, 9], which do not consider sequential hops. On the other hand, some works propose optimal hopping controllers for local maneuvers, but they rely on oversimplified dynamics models (e.g. a smooth surface or that bounces are deterministic) [10, 11]. This paper constitutes the first study of hopping traversability for small irregular bodies on a global scale.

3 DYNAMICS OF HOPPING ROVERS

The dynamics of hopping rovers can be decoupled into three parts: (1) the *hopping dynamics*, i.e. pushing off the surface, (2) *ballistic dynamics* of the rover in flight, and (3) *impact dynamics*, governing how the rover responds to surface collisions (see Fig. 2).

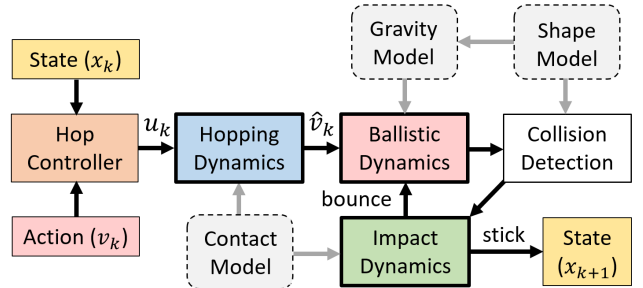


Figure 2: Flow chart of hopping dynamics. At rest on the surface at location x_k , the rover chooses a target hop velocity v_k and applies an appropriate control, u_k . Once in ballistic flight, which may last from seconds to hours, the rover eventually impacts the surface (possibly several times) before coming to rest at location x_{k+1} .

3.1 Hopping Dynamics

Without thrusters to steer it in flight, a hopping rover only has brief moments in which to control its motion—as it pushes off from the surface. In these few fractions of a second, it is unlikely that a hopper can use feedback control to achieve its desired launch velocity, v_k . Thus, the rover must estimate its pose and the local geometry and physical properties of the surface in order to apply an open-loop control action, u_k , that achieves v_k as closely as possible.

The details of the hopping dynamics for specific rover architectures are outside the scope of this paper (we refer the interested reader to [12], [4], and [13], for discussions of the dynamics of MINERVA, Hedgehog, and Asteroid hopper, respectively). Each hopping architecture has its own constraints on v , such as the maximum speed (v_{max}) and minimum elevation angle (θ_{min}) of a hop. Generally speaking, most hoppers that rely on surface reaction forces for control have a velocity cone constraint about the local surface normal governed by the friction properties of the surface (e.g. purple region in Fig. 3, left).

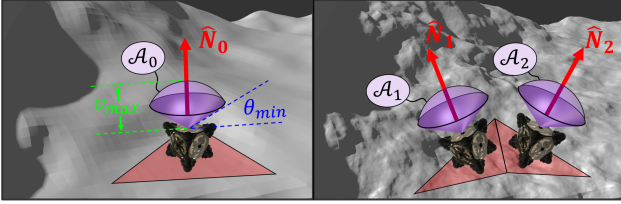


Figure 3: A coarse shape model (**left**) predicts that a rover has pose N_0 and associated action space \mathcal{A}_0 , whereas a finer shape model (**right**) reveals that the rover may have various poses (N_1, N_2) and action spaces ($\mathcal{A}_1, \mathcal{A}_2$) within the same region.

However, one particularly insidious challenge for trajectory planning is that the pose of the rover, which heavily influences its action space (\mathcal{A}), may not be aligned with the surface normal of the local facet in the shape model. Even very detailed global shape models with many millions of facets are unlikely to capture very fine surface features that affect the rover’s pose. Figure 3 illustrates how refined surface detail at the rover length scale can yield a fairly large distribution of poses that the rover may assume at a particular location. However, without prior knowledge of the local surface roughness within a facet, characterizing this distribution is infeasible. Therefore, we make the simplifying assumption that each triangular facet (and its associated normal vector) represents a local *average* of the true surface geometry and that a rover within this facet can reorient itself into this mean pose.

3.2 Ballistic Dynamics

Once in ballistic flight, the rover is subject to forces,

$$F = F_g - m [\omega_B \times (\omega_B \times x) + 2\omega_B \times v], \quad (1)$$

in the body frame, where F_g is the force of gravity, ω_B is the (constant) angular velocity of the body, and m , x , and v are the rover’s mass, position and velocity with respect to the body’s center of mass. Additional third-body forces may be required for binary asteroids or satellites like Phobos, but tertiary forces such as solar radiation pressure can often be neglected for short suborbital trajectories.

Gravity modeling near the surface of small bodies is challenging, as traditional spherical harmonic expansions diverge within the circumscribing sphere. Although computationally expensive, the most accurate gravity model on or near the surface is the constant density polyhedral model [14], possibly refined with an estimated internal density distribution [15]. In this paper, we leverage a reduced-order polyhedral model (about 5000 facets) to precompute the gravity at a regular 3D grid of points surrounding the body. In this way, simulations can integrate much more efficiently by interpolation (with very little sacrifice in accuracy).

3.3 Impact Dynamics

Finally, assuming a hop does not reach escape velocity, the rover will eventually impact the surface, at which point it

either bounces or sticks to the surface. Impact dynamics are highly dependent on the exact speed, spin, and pose of the rover upon contact as well as the geometry and physical properties of the surface at the point of contact, which are largely unobservable a priori. Thus, rebound velocities are highly stochastic and can only be characterized probabilistically. In Sect. 5, for the purposes of characterizing k -hop reachable sets, we assume that bouncing is minimal and that the rover lands at or nearby the first impact point. This assumption is reasonable if (1) the impact is sufficiently damped (practically, when restitution is below about 0.5), and (2) if the contact point is within a “geopotentially stable” region, i.e. that there are no considerable downward slopes nearby that would cause the hopper to accelerate away. In Sect. 5.2, we validate this assumption through simulations that include stochastic bouncing and other forms of model uncertainty.

4 SURFACE GRAVITY MAPS

In a typical mission scenario, before deploying a rover to the surface, an orbiting mother spacecraft would image the body from various viewing and lighting angles in order to estimate a shape model through stereophotoclinometry (SPC) or stereophotogrammetry (SPG), as was done for both the Hayabusa and Rosetta missions. Before even considering the dynamics of the rover, these shape models can be used to assess the traversability of the body at a global scale.

A shape model is defined by a closed triangular mesh consisting of n_v vertices, n_f triangular facets, and n_e edges. In this paper, we consider as a case study comet 67P, utilizing the 44-million facet model, “SPG SHAP7” developed by [16]. We compute the gravitational potential, acceleration, and gradient at each vertex based on a 5000-facet reduced order model as in [14]. Figure 4 shows three useful projections of this gravity information onto the surface: Geopotential, slope, and curvature.

Geopotential Maps: The effective potential (or “geopotential”) of a rotating body includes both its gravitational potential, $U_g(x)$, and the rotational potential, $U_r(x) = \frac{1}{2}\|\omega_B \times x\|^2$, where $U_{eff}(x) = U_r(x) + U_g(x)$. On a near-spherical (slowly rotating) body, the geopotential closely corresponds to the “height” (i.e. $1/r$), however it is not as simple or intuitive for bodies with complex shapes such as the bi-lobed comet 67P or fast rotating bodies such as Asteroid KW4α. Therefore, projecting the effective potential onto the surface (e.g. Fig. 4, left) is a useful tool for characterizing the gravitational highs and lows, or in other words, what regions are “uphill” and “downhill”—an important consideration for traversability. For example, the “Imhotep” region (the right portion of Fig. 4, bottom left image) is geometrically flat (i.e. close to a plane), however it is a geopotential basin, akin to a crater.

Note that unlike a spherical gravity model, geopotential is NOT necessarily correlated to the gravity magnitude. In

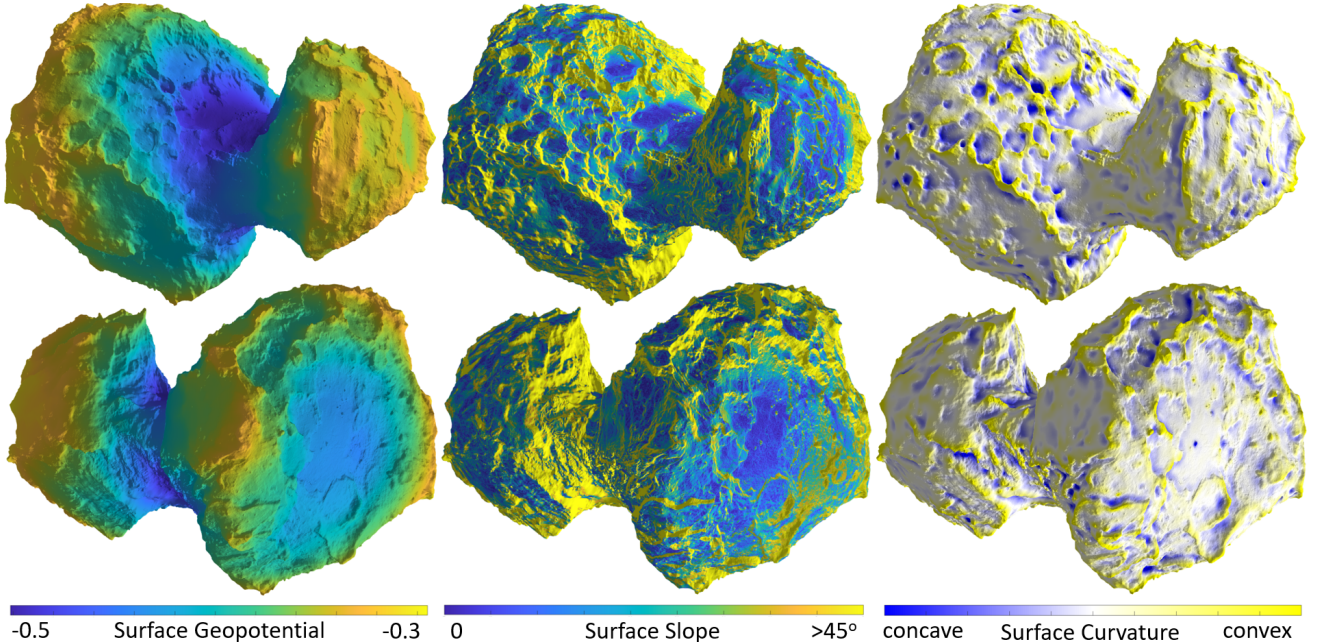


Figure 4: Surface gravity maps of comet 67P. Left: Surface geopotential (J/kg) highlights the energetic highs and lows on the surface. Center: Surface slope provides a map of “local levelness,” indicating where a rover may stably rest. Right: The geometric curvature of a body provides a measure of regional stability, whereby the scale of convexity/concavity of interest can be controlled via a local averaging kernel (here, $\sigma = 100\text{ m}$).

fact, the neck of comet 67P has the lowest geopotential and also the weakest gravity—the opposite of what a spherical gravity model predicts.

Slope Maps: The surface slope is defined for each facet, f_i , as $S_i = \cos^{-1}(-\hat{N}_i \cdot g_i / \|g_i\|)$, where \hat{N}_i is the outward unit normal vector of facet f_i and g_i is the effective gravity vector at the facet center (including centripetal acceleration). Surface slope is a crucial consideration when planning paths for traditional wheeled rovers, but it has a more fundamental implication for hoppers: it dictates where a hopper can even stably rest on the surface. A rover’s aspect ratio (i.e. the height of its CG over its base) imposes a maximum slope before it begins to tumble, and the surface friction imposes a maximum slope before it begins to slip, $S_{i,\max} = \tan^{-1}(\mu_i)$. Figure 4, center shows the surface slope map of comet 67P saturated at 45° —the maximum slope for the cubic Hedgehog rover. Although the actual surface geometry may vary within a facet (as discussed in Sect. 3.1) and facets themselves may have some error, slope maps are still quite useful for observing general slope trends.

Curvature Maps: While slope maps reflect the derivative of the surface potential, “curvature” is related to its second derivative—a measure of local *flatness*. Curvature is useful for characterizing regional stability, e.g., the tendency of a rover to diverge from convex regions and converge towards concave regions. There are many curvature metrics for triangulated meshes in the field of discrete differential geometry. Here, we use the “mean curvature”: a per-vertex vector measure of curvature with respect to neighboring fa-

cets [17]. We then compute the inner product of this curvature vector with the gravity vector to get a scalar metric oriented with the direction of changing geopotential.

However, the scale of a curvature metric based only on neighboring facets depends on the mesh resolution and may be too fine for global traversability considerations. Accordingly, we perform a local smoothing using an RBF kernel, which provides the ability to tune the curvature scale of interest by adjusting the RBF size ($\sigma = 100\text{ m}$ in Fig. 4, right). In the context of rover traversability, smoothed curvature can be thought of as a measure of *risk*, in that it can identify regions that are in close proximity to steep cliffs.

Other Maps: In addition to the three gravity maps discussed above, there are various other types of maps that might be considered for mission planning.

- **Region-of-interest (ROI)** maps are often the fundamental driver for rover mission planning as they directly encode mission objectives (e.g. sample collection sites for the Mars 2020 rover [6]).
- **Terrain classification** maps cluster visually similar regions such as rocky or regolith-covered regions, which can provide insight into potential physical properties of the surface as well as surface roughness that cannot be resolved through SPC or SPG shape modeling.
- **Rock abundance** maps can help to characterize rock size and frequency distributions across the surface.
- **Sun illumination** maps identify the lit regions of the surface at a particular time of day, or more generally,

the fraction of a day that the surface receives solar incidence. Illumination maps can be derived from traditional ray-tracing methods and may be very useful for rovers that rely on solar panels for recharging batteries or rovers with thermally sensitive instruments.

- **LOS Communication** maps, derived through a similar ray-tracing method as lighting, can identify where and when points on the surface are within line-of-sight (LOS) of the mother spacecraft for communication.
- **Localizability** maps encode the accuracy with which a rover can localize itself on the surface. For example, rovers that must establish feature correspondences between their onboard cameras and orbital imagery may perform better in well mapped and well lit regions [18].

4.1 Clustering Traversable Surface Regions

As discussed in Sec. 2, hopping has the potential to significantly expand the reachable portions of the surface by hopping over steep or rough terrain. However, before considering the reachability of hopping trajectories, we can first characterize locally traversable regions by simply examining the gravity maps. By making the assumption that a hopping rover can perform small controlled hops within regions of shallow surface slope, say $S < S_{max}$, we can leverage reachability properties from traditional surface motion planning to claim that “point x_2 is reachable from point x_1 if there exists a continuous path that connects x_1 to x_2 such that $S < S_{max}$ along the entire path.”

This two-dimensional planning problem is well suited for traditional combinatorial graph search algorithms (e.g.

Dijkstra or A^*), where the surface graph is naturally provided by the shape model with vertices representing nodes and their associated edge connectivity. Edges with a slope greater than S_{max} (or those with adjacent facets whose slope exceeds S_{max}) are removed from the graph and the connected components are decomposed into sub-graphs, or locally-traversable regions. The top row of Fig. 5 illustrates the connected regions of comet 67P for $S_{max} = 60^\circ$ (left), 40° (center), and 30° (right), and the bottom row shows heatmaps of the associated distance cost from a single location (star), overlaid with a tree of optimal trajectories.

Figure 5 shows just how challenging it would be for a wheeled rover—with slope limits typically less than 30° —to traverse comet 67P. However for hopping, we can leverage this surface decomposition to ease the global traversability analysis. Given our local traversability assumption above, we can now say that a point x_2 in region R_j is reachable from point x_1 in region R_i if there exists a feasible trajectory from *any* point in R_i to *any* other point in R_j . We leverage this surface decomposition for computing reachable sets in the next section.

5 REACHABILITY ANALYSIS

The escape velocity of small bodies is typically quite small—often less than a few m/s (e.g. 0.2 m/s on Itokawa and 1 m/s on comet 67P). Thus, it may often be possible to design a rover that can hop at sufficient speeds to traverse a significant portion of the surface in a single bound. In these “aggressive hopping” regimes, surface gravity maps alone may be insufficient to properly characterize the reachable regions of the surface. Additionally, it is important

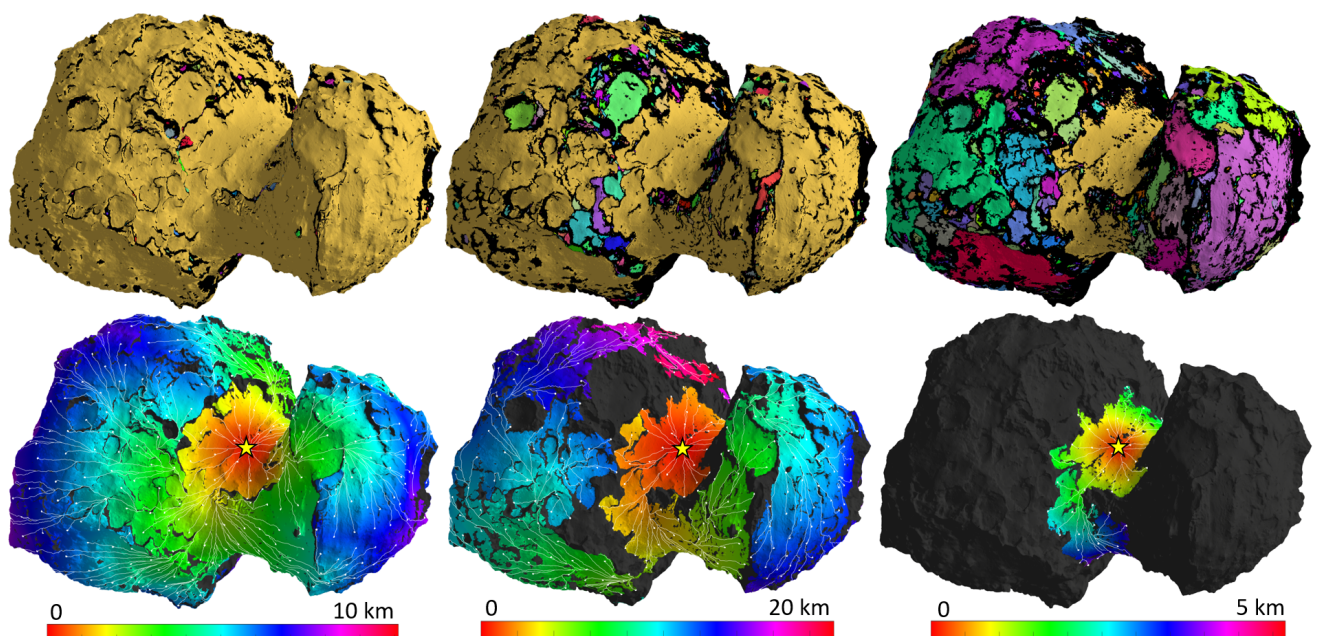


Figure 5: **Top:** Decomposition of surface into locally reachable regions, where $S < 60^\circ$ (**left**), $S < 40^\circ$ (**center**), and $S < 30^\circ$ (**right**). **Bottom:** Color maps corresponding to the travel distance from a point on the surface (star), superimposed with a tree of (distance-) optimal paths.

to consider the hopping *dynamics*, as discussed in Sect. 3.

In this section we propose a graph planning approach to compute forwards and backwards reachable sets to or from any arbitrary point on the surface by making the simplifying assumptions that (1) hops can be controlled exactly, (2) the gravity model is known, and (3) the rover does not bounce (Sect. 5.1). However, in Sect. 5.2, we show through Monte Carlo rollouts that these reachable sets and their associated control policies are robust to moderate levels of uncertainty in the control accuracy, gravity model, and bouncing dynamics.

5.1 Computing Reachable Sets

Computing the velocity, v_0 , required to reach a target point, x_f , from point x_0 in time T is Lambert’s famous orbital boundary value problem (BVP), which has no analytical solutions for highly irregular gravity fields. Moreover, the existence of solutions is not guaranteed since trajectories can be occluded by the irregular surface. Thus, we leverage a robust shooting method proposed by [8] to solve a finite set of BVP’s between a distributed set of points on the surface.

First, points from within the traversable regions (computed in Sect. 4.1) are sampled uniformly such that N points are maximally spaced and within some distance margin, d_{min} , from the perimeter¹. The number of samples required to sufficiently cover the surface depends on the maximum hop speed of the rover. In practice, N should be chosen such that the mean distance between neighboring points is less than half the rover’s maximum hop distance. The traversable regions of the surface (e.g. below some maximum slope) are then subdivided according to the “closest” sam-

¹This tunable heuristic biases samples towards the regions’ centroids.

ple within each region (see Fig. 6, left).

With a set of N uniformly distributed points on the surface, we then compute the solution to Lambert’s BVP between every pair of points within some “energetic radius,” $R_{max}(x_0, x_f) = \sqrt{v_{max}^2/\|g(x_0)\| - U(x_f) + U(x_0)}$ (see Fig. 6, center). This heuristic search radius roughly corresponds to the maximum distance of a projectile with speed v_{max} in a constant gravity field and significantly reduces the computational burden of solving all N^2 BVPs. According to the procedural Lambert shooting method in [8], we solve for the trajectory with the minimum velocity, $v_{0,min}(x_i)$ for each x_i (and its associated time, $T_{v_{min}}$), *without* checking for collisions. If this optimal trajectory is then found to be in collision with the surface, we slowly increment T until the solution is not in collision or until $v_0 > v_{max}$, in which case the BVP is infeasible. Figure 6, center shows a set of feasible trajectories for just one example point.

Finally, a directed graph is constructed among the N nodes, where edges e_{ij} represent feasible trajectories between nodes i and j and can be weighted according to a variety of metrics, including time, energy, or even the magnitude of the trajectory Jacobian—a measure of robustness (see [8] for details). A tree of optimal trajectories can then be readily computed to or from any target node in the graph (see Fig. 6, right).

The traversability graph is immediately useful for investigating a variety of mission design trade spaces. For example, edges in the graph can be systematically pruned according to constraints of various rover designs to observe the impact on reachability. Figure 7 illustrates one example study of how the maximum hop speed of a rover affects the time it takes to reach a target location. Similarly, we can probe the effects on reachability of prohibiting certain

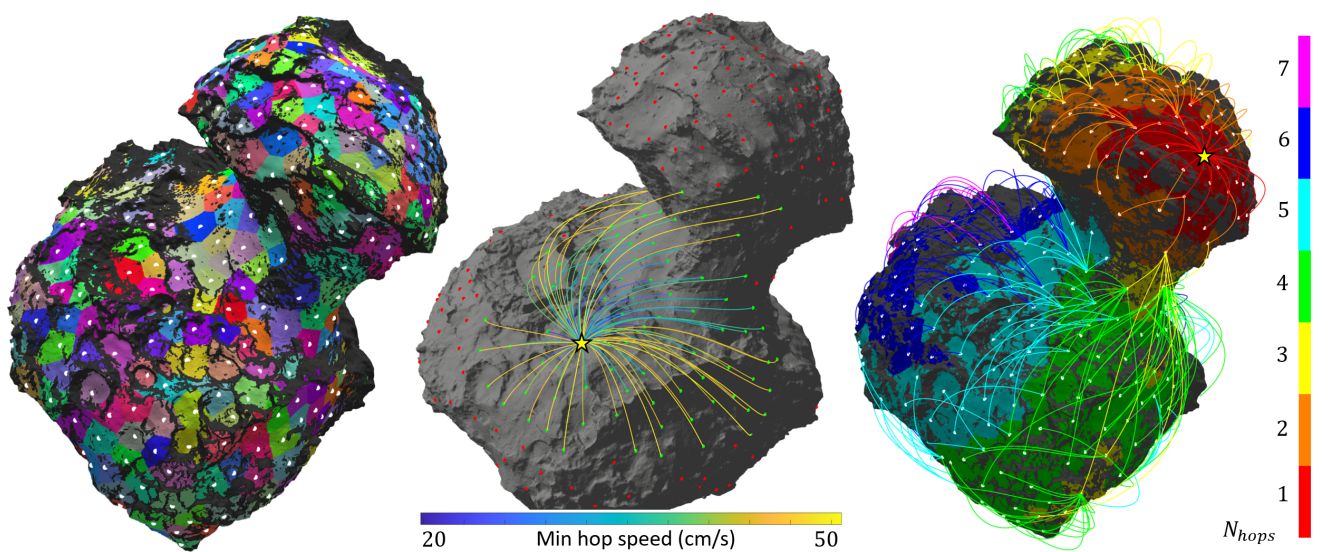


Figure 6: **Left:** The surface is sampled uniformly within the traversable regions (slope less than 30°). **Center:** The minimum-speed hop is computed from each point to every other point within its local neighborhood and a directed graph is constructed. **Right:** Edges are weighted (e.g. according to time or energy) and those that exceed the rover’s capabilities are removed (here, $v_{max} = 35$ cm/s). Finally, a tree of optimal trajectories can be computed to or from any node in the graph.

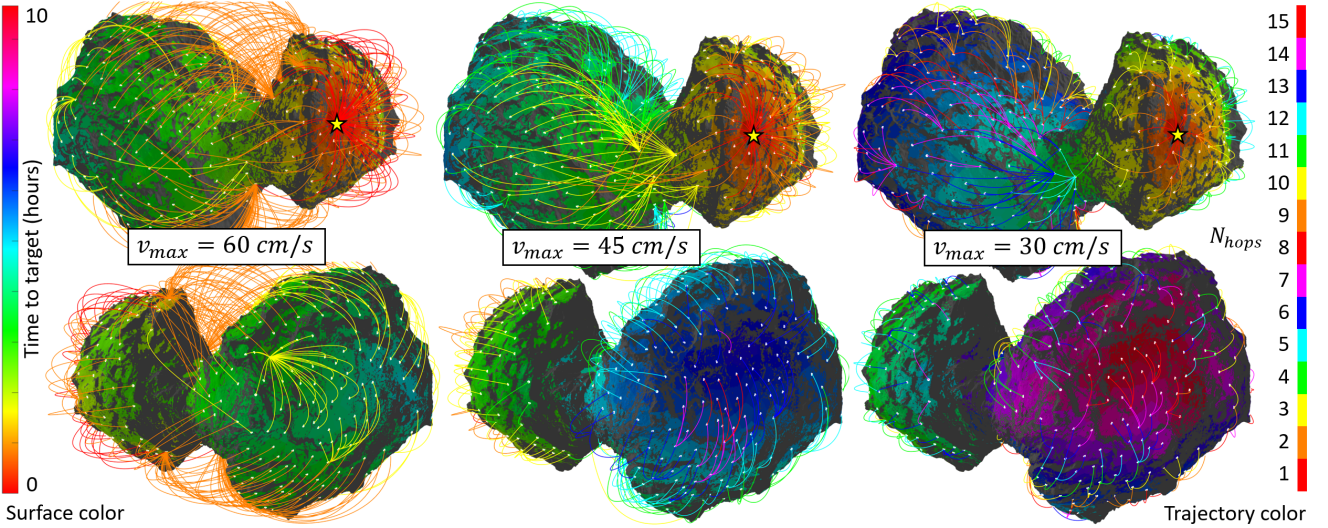


Figure 7: Time-optimal trajectory trees for a hopping rover with various speed constraints. The surface colormap reflects the optimal time to reach the goal and trajectory colors represent the number of hops remaining.

regions (e.g. due to communication or surface illumination constraints) by removing nodes from the graph. Also, given a set of target regions to visit, the graph could be used to determine the best location to deploy the rover or even the order in which to visit nodes by solving a traveling salesman problem (left for future work).

5.2 Numerical Validation

The reachability graphs computed in Sect. 5.1 are quite useful for rapid mission trade studies, but they are predicated on a simplified and deterministic dynamics model, and are thus, approximate. Due to various sources of uncertainty, including errors in the control, gravity model, and bouncing, these trajectories cannot be executed exactly. Here, we assess the performance of control policies generated by these graph search methods on systems with uncertainty through Monte Carlo simulations.

For this study, we consider two traverses: (1) from a low geopotential point on the neck of comet 67P to a high geopotential point on the head (i.e. an uphill traverse), and (2) the opposite, downhill traverse. For every hop, we take the action corresponding to the optimal edge of the nearest sample node in the graph and compute the exact Lambert solution to the corresponding target node. Gaussian noise is added to the hop velocity vector ($\Sigma_v = \sigma_v^2 I$, where $\sigma_v = 0.05 \|v_0\|$) to simulate control errors, and to the gravity field ($\sigma_g = 0.02 \|g\|$) to simulate uncertainty in the mass of the body. The dynamics are then propagated forward using a stochastic bouncing model with coefficient of restitution ranging from 0 to 0.9 (see [8] for details).

Figure 8 shows the mean realized time and number of hops to complete the traverse for 1000 Monte Carlo rollouts at each restitution level. For elastic collisions with a restitution of e , the nominal settling time of a hop can be estimated using the infinite series, $T(v_0, e) = T_{v_0} \sum_{n=0}^{\infty} e^n = T_{v_0}/(1 - e)$, where T_{v_0} is the time-of-flight for the first tra-

jectory. Thus, if bounces scatter uniformly around the impact point, the total “nominal traverse time” from x_1 to x_2 should roughly equal $T(x_1, x_2, e) = T_{\text{graph}}(x_1, x_2)/(1 - e)$, which is represented by the green line in Fig. 8, top. The fact that the uphill traverses are longer than this reflect the tendency of the hopper to bounce backwards, whereas the downhill traverses are aided by bounces.

The degree to which Monte Carlo rollouts resemble the optimal trajectory sequences derived in Sect. 5.1 depends on several factors—two of the most influential are impact elasticity and the change in geopotential across the traverse (i.e. moving uphill or downhill). These preliminary results suggest that, while it does not explicitly account for uncertainty in the dynamics, the graph-based reachability

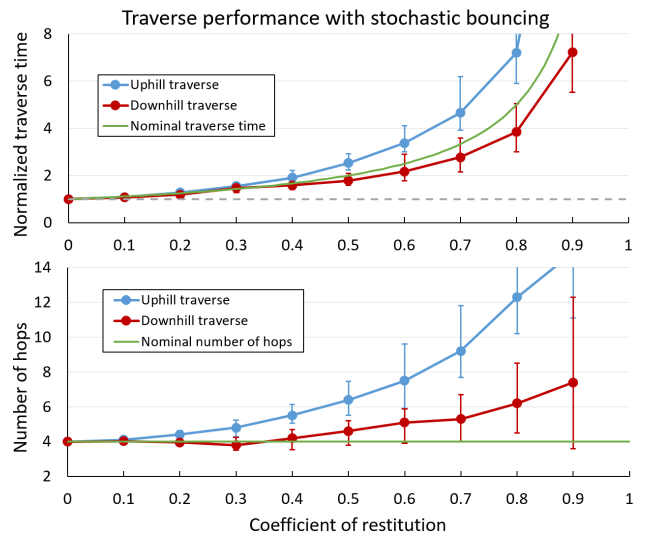


Figure 8: Mean normalized traverse time ($T/T_{\text{no bouncing}}$) and number of hops for 1000 Monte Carlo rollouts of the optimal graph-search policies across a range of impact elasticity (with 1σ error bars).

analysis presented in Sect. 5.1 may still be useful when the restitution is below about 0.5.

6 CONCLUSIONS

Future missions to small bodies will require enhanced surface mobility and autonomy. In this paper, we presented a set of tools to assess the global traversability of hopping rovers on small bodies with complex shape. We first discussed a suite of map-based tools that can be used to study the surface gravity environment of an arbitrarily shaped body and identify locally-traversable regions. We then employed a shooting solver to construct a graph of trajectories between a uniformly sampled set of points on the surface. We discussed how these traversability graphs can be used for a variety of mission trade studies and demonstrated through Monte Carlo simulations that they may even be applied where a moderate degree of bouncing is expected.

This work leaves numerous questions open for future investigations. Perhaps most important is the potential for these traversability graphs to compliment MDP-based planning methods. In particular, future work may consider a hybrid planning approach that leverages the speed and generalizability of the model-based methods presented here while also incorporating the robustness of uncertainty-aware MDP methods.

ACKNOWLEDGMENT

We would like to thank the King Abdul Center for Science and Technology (KAST) for their support through the Center of Excellence for Aeronautics and Astronautics (CEAA).

References

- [1] Castillo J, Pavone M, Nesnas I and Hoffman JA (2012) Expected Science Return of Spatially-Extended In-Situ Exploration at Small Solar System Bodies. In: *IEEE Aerospace Conference*.
- [2] Glassmeier KH, Boehnhardt H, Koschny E Dand Kührt and Richter I (2007) The Rosetta mission: flying towards the origin of the solar system. In: *Space Science Reviews*, 128(1):pp.1–21.
- [3] Kawaguchi J, Fujiwara A and Uesugi T (2008) Hayabusa—Its technology and science accomplishment summary and Hayabusa-2. In: *Acta Astronautica*, 62(10–11):pp.639–647.
- [4] Hockman B, Frick A, Nesnas IAD and Pavone M (2016) Design, Control, and Experimentation of Internally-Actuated Rovers for the Exploration of Low-Gravity Planetary Bodies. In: *Journal of Field Robotics*, 34(1):pp.5–24.
- [5] Hockman B, Reid RG, Nesnas IAD and Pavone M (2016) Experimental Methods for Mobility and Surface Operations of Microgravity Robots. In: *Int. Symp. on Experimental Robotics*.
- [6] Ono M, Rothrock B, Almeida E, Ansar A, Otero R, Huertas A and Heverly M (2016) Data-Driven Surface Traversability Analysis for Mars 2020 Landing Site Selection. In: *IEEE Aerospace Conference*.
- [7] Bajracharya M, Maimone MW and Helmick D (2008) Autonomy for Mars Rovers: Past, Present, and Future. In: *IEEE Computer*, 41(12):pp.44–50.
- [8] Hockman B and Pavone M (2017) Stochastic Motion Planning for Hopping Rovers on Small Solar System Bodies. In: *Int. Symp. on Robotics Research*.
- [9] Van wal S, Tardivel S and Scheeres DJ (2017) Parametric Study of Ballistic Lander Deployment to Small Bodies. In: *AIAA Journal of Spacecraft and Rockets*, 0(0):pp.1–26.
- [10] Bellerose J and Scheeres DJ (2008) Dynamics and Control for Surface Exploration of Small Bodies. In: *AIAA/AAS Astrodynamics Specialist Conference and Exhibit*.
- [11] Liu Y, Zhu S, Cui P, Yu Z and Zong H (2017) Hopping trajectory optimization for surface exploration on small bodies. In: *Advances in Space Research*, 60:pp.90–102.
- [12] Yoshimitsu T, Kubota T, Nakatani I, Adachi T and Saito H (2003) Micro-hopping robot for asteroid exploration. In: *Acta Astronautica*, 52(2–6):pp.441–446.
- [13] Fiorini P and Burdick J (2003) The Development of Hopping Capabilities for Small Robots. In: *Autonomous Robots*, 14(2):pp.239–254.
- [14] Werner RA and Scheeres DJ (1996) Exterior Gravitation of a Polyhedron Derived and Compared with Harmonic and Mascon Gravitation Representations of Asteroid 4769 Castalia. In: *Celestial Mechanics and Dynamical Astronomy*, 65(3):pp.313–344.
- [15] Takahashi Y and Scheeres DJ (2014) Morphology driven density distribution estimation for small bodies. In: *Icarus*, 233(1):pp.179–193.
- [16] Preusker F, Scholten F, Matz KD et al. (2017) The global meter-level shape model of comet 67P/Churyumov-Gerasimenko. In: *Astronomy and Astrophysics*, 607(L1).
- [17] Meyer M, Desbrun M, Schröder P and Barr AH (2003) Discrete Differential-Geometry Operators for Triangulated 2-Manifolds. In: *Visualization and Mathematics III*, pp.35–57.
- [18] Chiodini S, Reid RG, Hockman B, Nesnas IAD, Debei S and Pavone M (2018) Robust Visual Localization for Hopping Rovers on Small Bodies. In: *Proc. IEEE Conf. on Robotics and Automation*. In Press.